The Strength and Structure of the Magnetic Field in the Galactic Outflow of Messier 82

Enrique Lopez-Rodriguez[1,2] ⓘ, Jordan A. Guerra[3] ⓘ, Mahboubeh Asgari-Targhi[4] ⓘ, and Joan T. Schmelz[2,5]

[1] Kavli Institute for Particle Astrophysics and Cosmology (KIPAC), Stanford University, Stanford, CA 94305, USA; elopezrodriguez@stanford.edu
[2] SOFIA Science Center, NASA Ames Research Center, Moffett Field, CA 94035, USA
[3] Department of Physics, Villanova University, 800 E. Lancaster Avenue, Villanova, PA 19085, USA
[4] Harvard-Smithsonian Center for Astrophysics, 60 Garden Street MS-15, Cambridge, MA 02138, USA
[5] Universities Space Research Association (USRA), 7178 Columbia Gateway Drive, Columbia, MD 21046, USA

Abstract

Galactic outflows driven by starbursts can modify the galactic magnetic fields and drive them away from the galactic planes. Here, we quantify how these fields may magnetize the intergalactic medium (IGM). We estimate the strength and structure of the fields in the starburst galaxy M82 using thermal polarized emission observations from the Stratospheric Observatory for Infrared Astronomy/High-resolution Airborne Wideband Camera-plus and a potential field extrapolation commonly used in solar physics. We modified the Davis–Chandrasekhar–Fermi method to account for the large-scale flow and the turbulent field. Results show that the observed magnetic fields arise from the combination of a large-scale ordered potential field associated with the outflow and a small-scale turbulent field associated with bow-shock-like features. Within the central 900 pc radius, the large-scale field accounts for $53 \pm 4\%$ of the observed turbulent magnetic energy with a median field strength of $305 \pm 15~\mu$G, while small-scale turbulent magnetic fields account for the remaining $40 \pm 5\%$ with a median field strength of $222 \pm 19~\mu$G. We estimate that the turbulent kinetic and turbulent magnetic energies are in close equipartition up to $\sim$2 kpc (measured), while the turbulent kinetic energy dominates at $\sim$7 kpc (extrapolated). We conclude that the fields are frozen into the ionized outflowing medium and driven away kinetically. The magnetic field lines in the galactic wind of M82 are *open*, providing a direct channel between the starburst core and the IGM. Our novel approach offers the tools needed to quantify the effects of outflows on galactic magnetic fields as well as their influence on the IGM and evolution of energetic particles.

1. Introduction

Messier 82 (M82) is a canonical starburst galaxy at a distance of 3.85 ± 0.35 Mpc (20 pc arcsec^{-1}, Vacca et al. 2015, using SNIa 2014J). Observations reveal a bipolar superwind that originates in the core and extends perpendicular to the galactic plane out into the halo and intergalactic medium (IGM) (e.g., Shopbell & Bland-Hawthorn 1998; Lehnert et al. 1999; Ohyama et al. 2002; Engelbracht et al. 2006; Heckman & Thompson 2017). H_α emission line reveals an extended and continuous structure up to $\sim$11 kpc with an emission line structure in the northern region at $\sim$11–12 kpc, which is known as the *cap* (Devine & Bally 1999). The H_α is thought to be excited by radiation from the starburst region along the superwind. X-ray emission is observed at the location of the starburst region but also spatially coincident with the northern cap (Lehnert et al. 1999). X-ray emission is thought to be generated due to shock heating driven by the collisions between the superwind and massive ionized clouds in the halo of M82. The H_α-X-ray spatial correlation show evidence of this superwind driven material out of the galactic plane of M82.

The geometry of the magnetic fields in the core of the galaxy and the superwind has been investigated with various observing techniques. Nonthermal radio emission from the central region extends normal to the plane of M82, suggesting that the synchrotron emitting plasma is part of the outflow (Reuter et al. 1992). These results were obtained with the Very Large Array (VLA) from 3.6 cm to 90 cm at an angular resolution in the range of 4–35″. Subsequent observations with the VLA at 3.6 and 6.2 cm at a resolution of 15″ found

evidence for a poloidal magnetic field at heights of up to 400 pc from the plane, consistent with an outflowing plasma with velocities high enough to drag the field along with it (Reuter et al. 1994). These data from the VLA archive were later combined with complementary 18 and 22 cm data at a resolution of 15″ from the Westerbork Synthesis Radio Telescope (WSRT) by Adebahr et al. (2017). The analysis reveals polarized emission with a planar geometry in the inner part of the galaxy, which they interpret as a magnetized bar. The longer wavelength data show polarized emission up to a distance of 2 kpc from the disk, which could be described as large-scale magnetic loops in the halo.

Results from optical and near-IR (NIR) interstellar polarization observations suggest that the field geometry is perpendicular to the plane of this edge-on galaxy, in line with the superwind, rather than parallel as might be expected for spiral galaxies (see, e.g., Jones 2000, and references therein). However, polarimetry at optical and NIR wavelengths is strongly contaminated by the scattering of light from the nuclear starburst, and the relativistic electrons that give rise to the radio synchrotron emission may not sample the same volume of gas as polarization. Fortunately, the magnetic field structure can also be obtained using observations of polarized thermal emission from the aligned dust grains in the central region of M82. The field lines in the 850 μm polarization map with an angular resolution of 15″ from the Submillimetre Common-User Bolometer Array camera on the James Clerk Maxwell Telescope formed a giant magnetic loop or bubble with a diameter of at least 1 kpc. Greaves et al. (2000)

speculated that this bubble was possibly blown out by the superwind. However, a map created from reprocessed data with an angular resolution of 20″ did not show a clear bubble (Matthews et al. 2009).

Jones et al. (2019) analyzed far-IR (FIR) polarimetry observations of M82 at 53 and 154 μm with angular resolutions of 4.85″ and 13.6″, respectively, taken with the High-resolution Airborne Wideband Camera-plus (HAWC+; Vaillancourt et al. 2007; Dowell et al. 2010; Harper et al. 2018) on the Stratospheric Observatory for Infrared Astronomy (SOFIA). The polarization data at both wavelengths reveal a magnetic field geometry that is perpendicular to the disk near the core and extends up to 350 pc above and below the galactic plane. The 154 μm data add a component that is more parallel to the disk further from the nucleus. These results are consistent with the interpretation that the superwind outflow is dragging the field along with it.

The somewhat controversial nature of the magnetic bubble detected by Greaves et al. (2000) but not by Matthews et al. (2009) using the same data inspired us to draw upon a solar physics analogy. Would the HAWC+ field lines described by Jones et al. (2019) extend toward the IGM (galactic outflow), like the magnetic environment in the solar wind, or turn over to the galactic plane (galactic fountain), similar to coronal loops? To extend the HAWC+ data to greater heights above and below the galactic plane, we turn to a standard and well-tested technique used in heliophysics—the potential field extrapolation. With only rare exceptions (see, e.g., Schmelz et al. 1994, and references therein), the magnetic field in the solar corona, a magnetically dominant environment, cannot be measured directly. Therefore, significant effort has been invested by the community into extrapolating the field measured at the surface via the Zeeman effect up into the solar atmosphere. The simplest of these approximations assumes that the electrical currents are negligible so the magnetic field has a scalar potential that satisfies the Laplace equation and two boundary conditions: it reduces to zero at infinity and generates the normal field measured at the photosphere. The pioneering work by Schmidt (1964) assumed a flat photospheric boundary. Sakurai (1982) later expanded this technique to include a spherical boundary surface in a code that was available and widely used.

In this paper, we have quantified the magnetic field strength and structure in the starburst region of M82. We have also modified the solar potential field approximation to work with the HAWC+ data in order to extrapolate the magnetic field observed by Jones et al. (2019) and investigate the magnetic structures in the halo of M82. The paper is organized as follows: Section 2 describes the estimation of the averaged magnetic field strength in the starburst region, which we use to compute a two-dimensional map of the energies in Section 3. The potential field extrapolation is developed in Section 4. We discuss the results in Section 5 and conclusions in Section 6.

2. The Magnetic Field Strength of M82

2.1. The Davis–Chandrasekhar–Fermi (DCF) Method

The plane-of-the-sky (POS) magnetic field strength has been estimated from polarimetric data in Galactic (i.e., Wentzel 1963; Schmidt 1970; Gonatas et al. 1990; Zweibel 1990; Leach et al. 1991; Morris et al. 1992; Shapiro et al. 1992; Chrysostomou et al. 1994; Minchin & Murray 1994; Aitken et al. 1998;

Davis et al. 2000; Henning et al. 2001; Attard et al. 2009; Cortes et al. 2010; Chapman et al. 2011; Stephens et al. 2013; Cashman & Clemens 2014; Zielinski et al. 2021, Li et al., in preparation) and extragalactic sources (i.e., Lopez-Rodriguez et al. 2013, 2015, 2020) by using the classical DCF method (Davis 1951; Chandrasekhar & Fermi 1953). This method relates the line-of-sight (LOS) velocity dispersion and the POS polarization-angle dispersion. It assumes an isotropically turbulent medium, whose turbulent kinetic and turbulent magnetic energy components are in equipartition.

For a steady state with no large-scale flows, the DCF method establishes that the velocity of a transverse magnetohydrodynamical (MHD; Alfvén) wave,

$$V_A = \frac{B}{\sqrt{4\pi\rho}}, \tag{1}$$

is related to the observed dispersion of polarization angles, where B is the magnetic field strength and ρ is the mass density. This relation is derived from the wave equation with the propagation velocity found to be

$$V^2 = V_A^2 = \frac{\sigma_v^2}{\sigma_\phi^2}, \tag{2}$$

where σ_v is the amplitude of the time variation (i.e., velocity dispersion) and σ_ϕ is the spatial amplitude (i.e., angular dispersion). Combining Equations (1) and (2), gives us the well-known DCF approximation:

$$B_{\mathrm{DCF}} = \xi\sqrt{4\pi\rho}\,\frac{\sigma_v}{\sigma_\phi}. \tag{3}$$

The angular dispersion σ_ϕ is the standard deviation of the distribution of polarization angles. When $\sigma_\phi \leqslant 25°$, $\xi \sim 0.5$ accounts for the projection of the magnetic field and density distributions on the POS (Ostriker et al. 2001).

Figure 1 shows the magnetic field orientations of M82 inferred from the 53 μm observations with HAWC+ (Jones et al. 2019). Polarization measurements with $P/\sigma_P \geqslant 2$ are shown, where σ_P is the uncertainty of the polarization fraction, P. Polarization measurements have been normalized and rotated by 90° to show the B-field orientation. To apply the DCF approximation, the velocity dispersion, mass density, and angular dispersion have to be estimated in the same region. We perform our DCF analysis within the starburst region generated using the gas kinematics in the superwind (Figure 18 from Contursi et al. 2013). Specifically, the FIR spectroscopic analysis of Contursi et al. (2013) separated the kinematics of M82 into four regions—the disk, the starburst, the northern outflow, and the southern outflow—based on several emission lines ([C II], [O I], and [O III]) using PACS/Herschel data. We find that only the starburst region provides sufficient polarization measurements to perform the dispersion analysis used for this work. The starburst mask, with a size of 873×510 pc^2 at a position angle (PA) of ~69° in the east of north direction, the region of focus for this work, is shown in Figure 1.

Figure 2 (top) shows the maps of the several empirical quantities necessary to estimate the magnetic field strength within the starburst mask. Figure 2 (bottom) shows the distributions of each quantity with the estimated median (solid line) and 1σ uncertainties (dashed lines). The first is the column density, $N_{\mathrm{H+H_2}}$, from Jones et al. (2019). The $N_{\mathrm{H+H_2}}$ map has been smoothed using a Gaussian profile with an FWHM equal
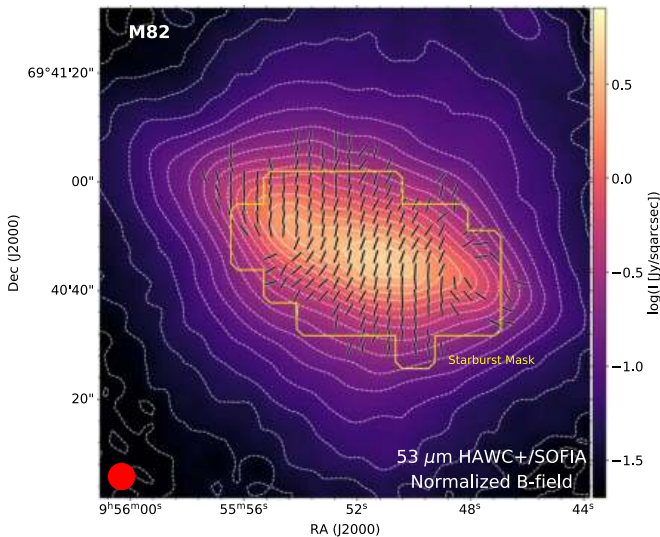
Figure 1. Inferred magnetic field orientation (black) of M82 using the 53 μm polarimetric observations with HAWC+/SOFIA (Jones et al. 2019). All polarization measurements are normalized to unity, and only those with $p/\sigma_P \geqslant 2$ are shown. The color scale shows the total intensity at 53 μm. Contours start at 4σ with increments of $2^{n\sigma}$, where $n = 2.0, 2.5, 3.5,...$ and $\sigma = 2.52$ mJy arcsec^{-2}. The starburst mask (yellow solid line), with a size of 873×510 pc^2 at a PA of $\sim69°$, taken from (Contursi et al. 2013, Figure 18) is used for the parameter estimations of the magnetic field strengths. Beam size (red circle) is shown.

to the beam size of the HAWC+ observations and projected to the HAWC+ observations. We estimate the median column density within the starburst mask to be $N_{H+H_2} = (2.27 \pm 0.57) \times 10^{22}$ cm^{-2}. To convert N_{H+H_2} to mass density (ρ), we need to know the extend of the gas and dust in the LOS direction. An estimate of this dimension is the effective depth of the starburst region, Δ', which can be calculated following Houde et al. (2011). Specifically, we calculate the normalized autocorrelation function of the polarized flux of M82 using polarization measurements with $P/\sigma_P \geqslant 3$. This cut ensures that the same polarization measurements are used through the data analysis. Then, the half width at half maximum of the distribution is taken as the value of Δ', which is estimated to be $\Delta' = 0\!.\!1613$ (193.6 pc). We interpret Δ' as the depth of the starburst region that contains $\geqslant 50\%$ of the polarized flux, which assumes that the gas and dust distribution in the starburst of M82 is isotropic. Note that this estimation does not use a filling factor of the dust within the starburst region. Our result is in good agreement with that of Adebahr et al. (2017), who estimated a width of the polarized emitting region of ~250 pc using 3 and 6 cm data and assuming a cylindrical symmetry. Finally, using Δ', we can estimate the mass density within the starburst mask to be $\rho = m_H \mu N_{H+H_2}/\Delta' = (1.78 \pm 0.45) \times 10^{-22}$ g cm^{-3}, where m_H is the hydrogen mass and $\mu = 2.8$ is the mean molecular mass.

Multiple authors have measured the velocity dispersion for the central disk of M82 within similar physical scales as our mask. Emission lines, e.g., [ArIII] 8.99 μm, H$_2$ 17.034 μm, [FeII] 25.98 μm, and [SiII] 34.815 μm, in the mid-infrared observed with the Infrared Space Observatory and an angular resolution of 9″ (180 pc) show velocities within a range of $71-114$ km s^{-1} (Sohn et al. 2001). ^{12}CO(1-0) observations made with the Nobeyama Millimeter Array at a resolution of 2.5″ (50 pc) show a velocity dispersion of 89 km s^{-1}

(Chisholm & Matsushita 2016). Tadaki et al. (2018) measured the velocity dispersion of individual clumps in the disk of M82 to be ~100 km s^{-1} using 0.05″ resolution CO observations with the Atacama Large Millimeter/submillimeter Array. They also estimated a velocity dispersion of 74 ± 1 km s^{-1} for the CO-emitting gas within a disk of ~1 kpc radius. Understanding that the velocity dispersion of the disk shows a very complex structure, we find that the most complementary observations for our analysis come from Leroy et al. (2015). They show that the molecular gas, ^{12}CO(2–1), traces the high-density regions of M82, which is spatially coincident with the dust emission from our FIR observations. We use their ^{12}CO(2–1) emission line within our mask, which we smoothed using a Gaussian profile with an FWHM equal to the beam size of the HAWC+ observations and projected to the HAWC+ observations. We estimate a median velocity dispersion of $\sigma_{v,^{12}CO(1-2)} = 66.0 \pm 6.6$ km s^{-1} (Figure 2).

The final variable required to estimate B_{DCF} is σ_ϕ, which corresponds to the standard deviation of the polarization-angle distribution. Here, we use the polarization angle of the inferred B-field orientation from the 53 μm HAWC+ observations (Jones et al. 2019) within our mask to estimate a median value of $-15.3°$ with an angular dispersion (s.d.) of $\sigma_\phi = 17.1°$. Within the mask, 17% of polarization measurements have a P/σ_P between 2 and 3, with a median $P/\sigma_P = 8$. Thus, the angular dispersion is larger than the uncertainty related to the polarization measurement. Therefore, using $\sigma_\phi = 0.29$ rad (17.1°), we find $B_{DCF} = 0.54 \pm 0.17$ mG.

2.2. The Angular Dispersion Function

In the starburst region of M82, the dominant driver of the turbulence is the supernova explosions. The observed patterns of the B-field orientation are the results of two contributions: (1) one from the morphology of the large-scale regular magnetic field, which is larger than the turbulent scale (δ) driven by supernova explosions at scales of 50–100 pc in nearby galaxies (i.e., Ruzmaikin et al. 1988; Elmegreen & Scalo 2004; Brandenburg & Subramanian 2005; Haverkorn et al. 2008) and (2) another contribution from the small-scale (i.e., turbulent or random) magnetic field, which relies on turbulent gas motions at scales compared to or smaller than δ. Because the DCF method relies on the speed of an Alfvén wave to measure the magnetic field strength, only the perturbed (i.e., turbulent or random) component provides the correct value of B. Therefore, it is important to extract the turbulent component from the measured dispersion.

Hildebrand et al. (2009) and Houde et al. (2009, 2011) have been able to separate the regular and turbulent components using a careful analysis of the dispersion of polarization angles obtained from dust continuum polarization observations. This technique has been applied to FIR-submillimeter polarimetric observations of Galactic sources (i.e., Chapman et al. 2011; Crutcher 2012; Girart et al. 2013; Pattle et al. 2017; Chuss et al. 2019; Redaelli et al. 2019; Soam et al. 2019; Wang et al. 2020; Guerra et al. 2021; Michail et al. 2021, Li et al. in preparation), as well as submillimeter polarimetric observations of external galaxies, like M51 (Houde et al. 2013). Specifically, an isotropic two-point structure function (i.e., dispersion function) is computed to describe the dispersion as a function of angular scale. Then, the dispersion function separates the large-scale field from that of the turbulence (Houde et al. 2016,
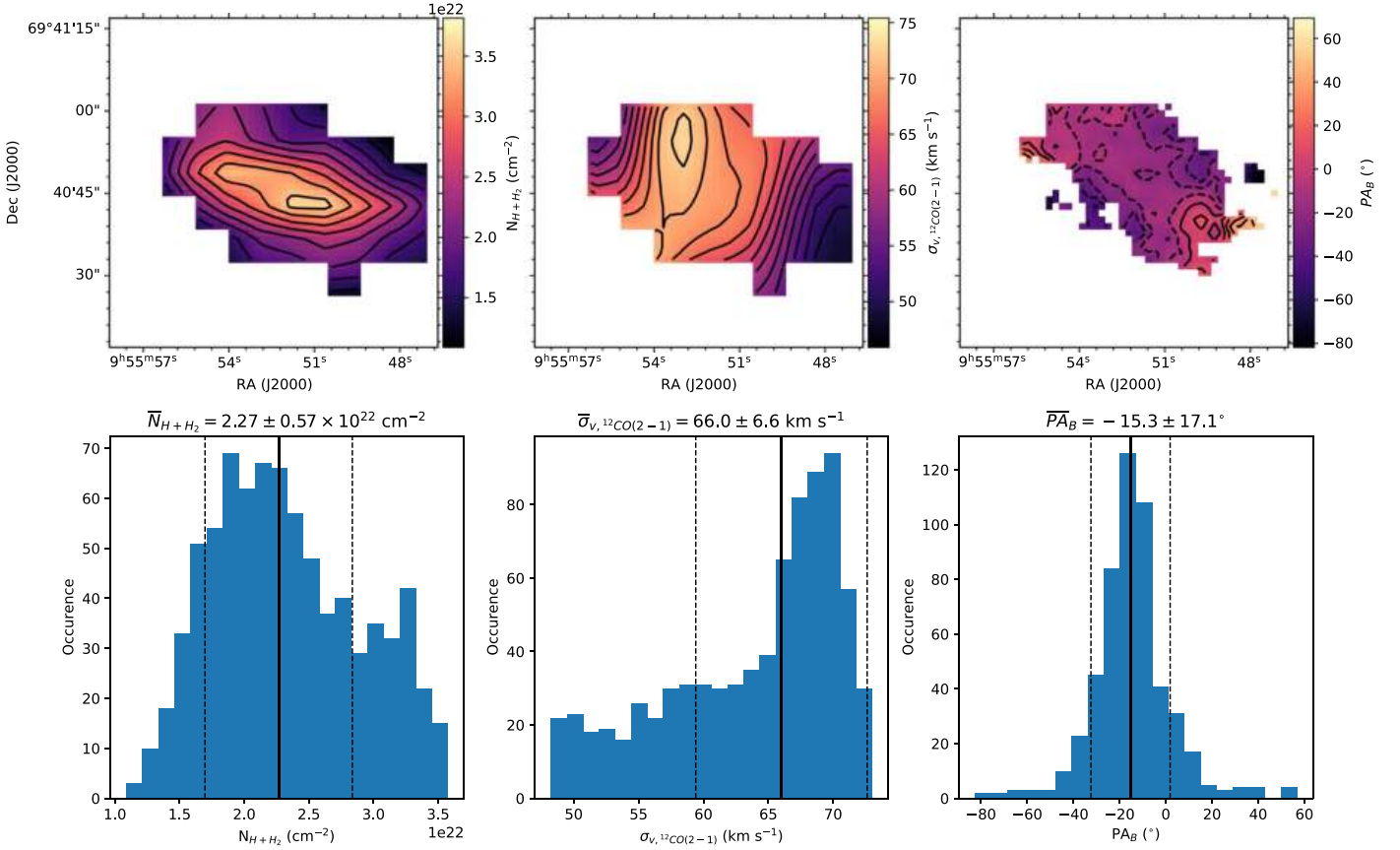
Figure 2. Top: maps of the $N_{\mathrm{H}+\mathrm{H}_2}$ (left) from Jones et al. (2019), $\sigma_{v,^{12}\mathrm{CO}(1-2)}$ (middle) from Leroy et al. (2015), and PA of the inferred B-field orientation, PA$_B$, (right) using the 53 μm polarimetric observations from Jones et al. (2019). Contours start at $N_{\mathrm{H}+\mathrm{H}_2} = 1.09 \times 10^{22}$ cm^{-2} and $\sigma_{v,^{12}\mathrm{CO}(1-2)} = 48$ km s^{-1}, and increase in steps of 0.3×10^{22} cm^{-2} and 2 km s^{-1}, respectively. The contours of PA$_B$ are displayed in the range of [-90°,90°] in intervals of 10°. Bottom: histograms of the measurements for each map. The median (solid line) and 1σ uncertainties (dashed lines) are shown.

Equation (13)),

$$1 - \left\langle \cos[\Delta\phi(l)] \right\rangle = \frac{1}{1 + \mathcal{N} \left[\frac{\langle B_t^2 \rangle}{\langle B_0^2 \rangle} \right]^{-1}}$$
$$\times \left\{ 1 - \exp\left(-\frac{l^2}{2(\delta^2 + 2W^2)} \right) \right\} + a_2 l^2, \quad (4)$$

where the first term on the right accounts for the small-scale turbulent contribution to the dispersion, and the second term accounts for the large-scale regular (ordered) field contribution. l is the distance between pairs of measurements with angle difference $\Delta\phi$. W is the standard deviation of the beam size assumed to be a Gaussian function $W = \mathrm{FWHM}\,/2.355 = 2.05''$, where FWHM $= 4.85''$ for our 53 μm HAWC+ observations (Harper et al. 2018). $\langle B_t^2 \rangle / \langle B_0^2 \rangle$ is the turbulent-to-large-scale energy ratio, δ is the correlation length for the turbulent field, a_2 is the large-scale coefficient, and $\mathcal{N}$ is the number of independent turbulent cells in the column of dust probed observationally given by

$$\mathcal{N} = \frac{(\delta^2 + 2W^2)\Delta'}{\sqrt{2\pi}\,\delta^3} \quad (5)$$

(Houde et al. 2016, Equation (14)), where Δ' is the effective thickness of the starburst region, which was already estimated in Section 2.1.

We evaluate the left-hand side of Equation (4) within the starburst mask using the 53 μm polarization data of M82 observed with HAWC+ (Jones et al. 2019). Using $\Delta' = 0.'1613$ (193.6 pc), this leaves three free parameters to be determined: $\langle B_t^2 \rangle / \langle B_0^2 \rangle$, δ, and a_2. We use a Markov Chain Monte Carlo (MCMC) solver for fitting the nonlinear model of Equation (4) to the dispersion functions as implemented by Chuss et al. (2019). This fitting routine infer the optimal model parameters and its associated uncertainties from the posterior distributions of the MCMC chains. Figure 3 (left) shows the separation of the two components in the measured dispersion function $1 - \left\langle \cos[\Delta\phi(l)] \right\rangle$. Panels (a) and (b) show in blue circles the measured values of $1 - \left\langle \cos[\Delta\phi(l)] \right\rangle$ and the best fit (red solid line) for the large-scale component (term $\propto \ell^2$ in Equation (4)), which is valid only for $\ell \gtrsim 0.18$ arcmin. For $\ell \lesssim 0.18'$, the turbulent component dominates, which is then analyzed in panel (c). In panel (c), blue circles correspond to the autocorrelated turbulent component $(1 - \left\langle \cos[\Delta\phi(l)] \right\rangle - a_2 \ell^2)$, which is valid only for the smaller scales and is fit (red dashed line) using the first term in Equation (4). The turbulent component is compared with autocorrelated beam profile (solid gray line). Correctly accounting for the gas turbulence in the polarization-angle dispersion depends on the autocorrelated turbulent component having a wider shape than the observations' autocorrelated beam. This is evident in Figure 3(c). Figure 3 (right) shows the posterior distributions obtained with the MCMC solver, whose
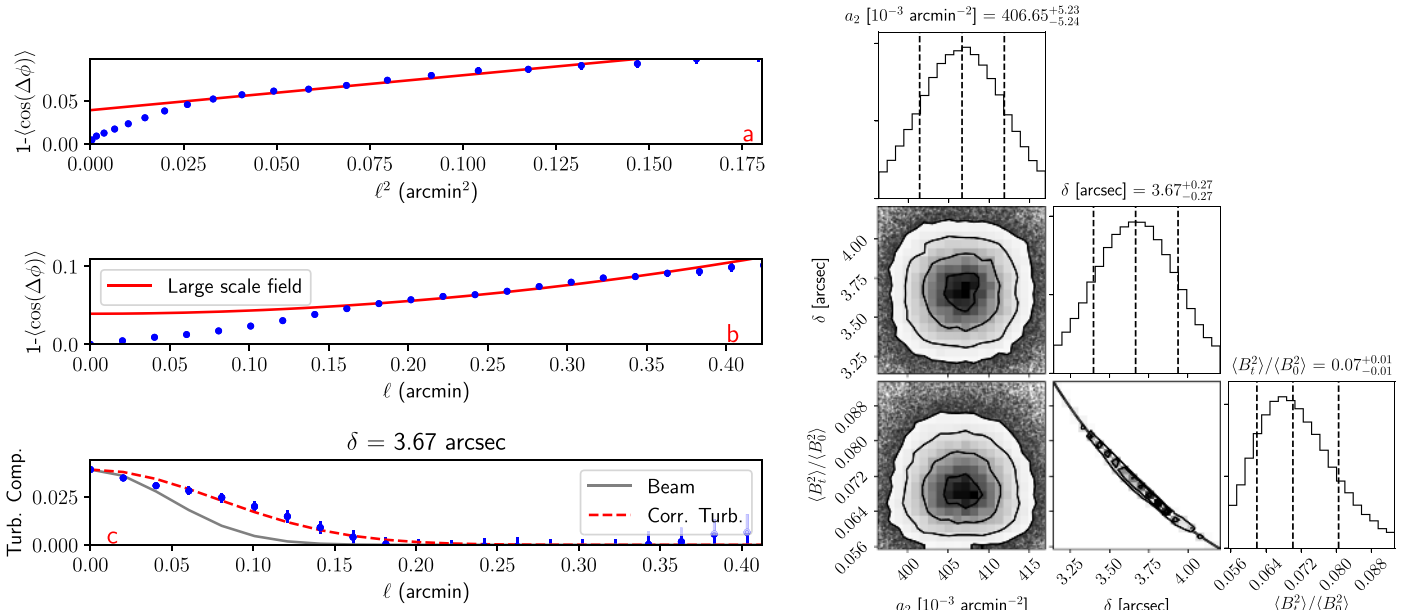
Figure 3. Left: dispersion functions (a) and (b) within the starburst mask of M82 at 53 μm. Data points (blue circles) and fits (red solid line) of the large-scale field are shown. (c) The best fit (red dashed line) of the turbulent component and the beam (gray solid line) of the observations are shown. The fits represent the best inferred results using Equation (4). Right: posterior distributions of the large-scale field (a_2), turbulent correlation length (δ), and turbulent-to-large-scale field ratio ($\langle B_t^2 \rangle / \langle B_0^2 \rangle$).

statistics provide the best-fit model parameter values for the dispersion function with $a_2 = 406.65^{+5.23}_{-5.24} \times 10^{-3}$ arcmin^{-2}.

We infer a coherent length of the turbulent magnetic field to be $\delta = 3''67^{+0.27}_{-0.27}$ (73.6$^{+5.6}_{-5.6}$ pc). The coherent length is larger than the beam size of our observations (Figure 3(c)), $\sqrt{2}W = 2.90''$, which allow the characterization of the turbulent magnetic field (Houde et al. 2011). It is worth noting that our coherent length of the turbulent magnetic field is in agreement with the typical scale length of turbulent fields in galaxies of order 50–100 pc, which is driven by supernova explosions (i.e., Haverkorn et al. 2008). Adebahr et al. (2017) estimated a coherent length of the magnetic field of ~50 pc using radio polarimetric observations in the central ~1 × 0.7 kpc^2 of M82, in agreement with our results. Using isotropic Kolmogorov turbulence ($P(k) \propto k^{5/3}$), we estimate a coherent length (López-Coto & Giacinti 2018) of $L_c = \delta/5 = 14.7$ pc, where δ is considered to be the maximum coherent length, L_{max}, within the starburst region. We conclude that our observations are able to resolve the turbulent magnetic field in the central 873 × 510 pc^2 starburst of M82 and therefore, further detailed analysis of the magnetic field strengths can be performed.

We infer a turbulent-to-large-scale energy of $\langle B_t^2 \rangle / \langle B_0^2 \rangle = 0.07^{+0.01}_{-0.01}$. This result implies that the central starburst region of M82 is dominated by a large-scale ordered magnetic field since the turbulent magnetic energy is small (≈7%) in comparison. We quantify the effect of the galactic outflow in Section 2.3.

We can now estimate the POS magnetic field strength using the angular dispersion function (ADF) as

$$B_{ADF} = \sqrt{4\pi\rho}\, \sigma_v \left[\frac{\langle B_t^2 \rangle}{\langle B_0^2 \rangle} \right]^{-1/2} \quad (6)$$

(Houde et al. 2009). The values of ρ, the mass density, and σ_v, the velocity dispersion, are those previously estimated in Section 2.1 and Figure 2. Using these parameters, we estimate

the magnetic field strength within the starburst mask of M82 to be $B_{ADF} = 1.04 \pm 0.17$ mG.

2.3. The Effect of Galactic Outflows

In this section, we investigate how both values of the magnetic field, B_{DCF} and B_{ADF}, are affected by the M82 outflow. Assuming there is a steady, large-scale velocity field $U_0 = U_0 \hat{z}$ in the same direction as the magnetic field B, the wave equation for this case—after several steps—reduces to (Equation (10) by Nakariakov et al. 1998):

$$\left[\frac{\partial}{\partial t} + (U_0 - V_A)\frac{\partial}{\partial z} \right]\left[\frac{\partial}{\partial t} + (U_0 + V_A)\frac{\partial}{\partial z} \right] V = 0. \quad (7)$$

This means there are two standing waves with velocities $V^- = U_0 - V_A$ and $V^+ = U_0 + V_A$. However, these two velocities are associated with the same observed spatial disturbance (i.e, polarization-angle dispersion). Replacing this modified velocity into Equation (2),

$$(V^\pm)^2 = (U_0 \pm V_A)^2 = \frac{\sigma_v^2}{\sigma_\phi^2} \quad (8)$$

results in

$$\pm V_A = \frac{\sigma_v}{\sigma_\phi} - U_0. \quad (9)$$

Using the definition of the Alfvén wave (Equation (1)),

$$\pm \frac{B}{\sqrt{4\pi\rho}} = \frac{\sigma_v}{\sigma_\phi} - U_0, \quad (10)$$

which indicates that two Alfvén waves with the same speed travel in opposite directions, due to the same magnetic field strength and the same nonzero, steady-state, large-scale velocity. Therefore, we can take the absolute value of

Equation (10) and rearrange the terms,

$$B = \sqrt{4\pi\rho} \left| \frac{\sigma_v}{\sigma_\phi} - U_0 \right|, \tag{11}$$

where B is the absolute value of the field strength. Finally, using the definition of B_{DCF} (including the adjustment factor ξ), we define the modified B'_{DCF} as

$$B'_{\mathrm{DCF}} = B_{\mathrm{DCF}} \left| 1 - \sigma_\phi \frac{U_0}{\sigma_v} \right|. \tag{12}$$

Equation (12) reduces to the well-known DCF approximation (Equation (3)) when $U_0 = 0$. Assuming, of course, that σ_ϕ is nonzero, the modification to the DCF value is proportional to U_0/σ_v—the ratio of large-scale velocity to the velocity dispersion.

From Equation (12) we now have two possible regimes:

1. $B'_{\mathrm{DCF}} < B_{\mathrm{DCF}}$, which means $\sigma_\phi \frac{U_0}{\sigma_v} < 2$ and $\neq 1$.
2. $B'_{\mathrm{DCF}} > B_{\mathrm{DCF}}$, which means $\sigma_\phi \frac{U_0}{\sigma_v} > 2$.

Therefore the correction to the DCF value (Equation (12)) increases the strength of the magnetic field when the ratio of dispersion-to-large-scale velocities is lower than half the measured angle dispersion ($0.5\sigma_\phi > \sigma_v/U_0$)—the large-scale velocity field dominates. On the other hand, the correction lowers the magnetic field strength when the turbulence dominates the velocity field ($0.5\sigma_\phi < \sigma_v/U_0$).

Using the median velocity of the $^{12}\mathrm{CO}(2-1)$ molecular outflow within the starburst mask of $U_0 = 396 \pm 87$ km s^{-1} (Leroy et al. 2015), the $\sigma_\phi = 0.29$ rad, and $\sigma_v = 66.0 \pm 6.6$ km s^{-1} from Section 2.1, we estimate the modifying factor to be

$$\sigma_\phi \frac{U_0}{\sigma_v} = 1.74 \pm 0.42. \tag{13}$$

Since this factor is <2, we conclude that the large-scale velocity field from the galactic outflow dominates over the turbulent magnetic field within the starburst mask. This result is in agreement with the large-scale regular magnetic field dominating over the turbulent magnetic energy within the starburst region. These results imply that the B_{DCF} and B_{ADF} are overestimated. We can now calculate the corrected strength of the magnetic field within the starburst mask for both the classical DCF method, $B'_{\mathrm{DCF}} = 0.40 \pm 0.26$ mG, and the angular dispersion analysis method, $B'_{\mathrm{ADF}} = 0.77 \pm 0.17$ mG.

Both estimates of the magnetic field, B'_{DCF} and B'_{ADF}, agree within the uncertainties when a galactic outflow component is taken into account. The separation of turbulent-to-large-scale fields, as described in Houde et al. (2009), does take into account some influence of the large-scale velocities present in the starburst mask. However, the ADF method still requires a correction of $\sim 25\%$. As the corrected ADF method is now dominated by the turbulent field, we use B'_{ADF} hereafter.

3. The Two-dimensional Map of the Magnetic Field Strength

In Section 2, we estimated the average turbulent magnetic field strength in the starburst region of M82 using the mean of the mass density, velocity dispersion, and angular dispersion. Here, we estimate the pixel-by-pixel turbulent magnetic field

strength using the full maps of the mass density and velocity dispersion. A similar approach has successfully been applied to the Orion nebula (OMC-1) by Guerra et al. (2021). We here present a novel approach using the energy budget to estimate the two-dimensional turbulent magnetic field strength of M82.

Contursi et al. (2013) suggested that the cold clouds from the disk are entrained into the outflows by the galactic wind, where small, dense clouds may remain intact during the outflow process. Jones et al. (2019) proposed a scenario where the magnetic field is entrained within the gas and dust, and dragged by the outflow away from the galactic disk together with the galactic wind. This entrainment is generally quantified by the plasma β parameter, defined as the ratio of thermal gas pressure, U_G, to magnetic pressure, U_B. β traditionally determines whether an environment is dominated by thermal or magnetic forces:

$$\beta = \frac{U_G}{U_B} = \frac{n_H k_B T_g}{B^2/8\pi}, \tag{14}$$

where n_H is the gas density, k_B is the Boltzmann constant, and T_g is the gas temperature.

Turbulent energy densities are generally larger than thermal energy densities in galaxies (Beck & Krause 2005). Thus, a β−like parameter that takes both the turbulent kinetic and hydrostatic energies of the outflow of M82 into account is required. We here define a β' parameter:

$$\beta' = \frac{U_H + U_K}{U_B}, \tag{15}$$

where U_H, U_K, and U_B are the hydrostatic, turbulent kinetic, and turbulent magnetic energies, respectively.

Let the hydrostatic energy, U_H, be

$$U_H = \pi G \Sigma_g^2 = \pi G (N_H m_H \mu)^2 \tag{16}$$

where G is the gravitational constant, Σ_g is the gas density, N_H is the gas column density, m_H is the hydrogen mass, and $\mu = 2.8$ is the mean molecular mass per H molecule.

Let the turbulent kinetic energy, U_K, and magnetic energy, U_B, be

$$U_K = \frac{1}{2}\rho\sigma_v^2 \tag{17}$$

$$U_B = \frac{B^2}{8\pi} \tag{18}$$

where σ_v is the three-dimensional dispersion velocity defined as $\sqrt{3}\,\sigma_{v,^{12}\mathrm{CO}(2--1)}$.

Using β' (Equation (15)), the two-dimensional magnetic field strength map can be estimated such as

$$\begin{aligned} B &= \left[8\pi \left(\frac{U_K + U_H}{\beta'} \right) \right]^{1/2} \\ &= \left[\frac{8\pi}{\beta'} \left(\pi G N_H m_H \mu + \frac{1}{2}\rho\sigma_V^2 \right) \right]^{1/2}, \end{aligned} \tag{19}$$

where we impose the condition that β' is equal to the mean value of the energies within the starburst mask.

We use the mean values within the starburst mask from Section 2, and estimate a $\beta' = 0.56 \pm 0.23$. Imposing this condition satisfies that the estimated mean turbulent magnetic field strength within the starburst mask is $\langle B \rangle = B'_{\mathrm{ADF}} = 0.77$ mG. In combination with the maps of $N_{\mathrm{H}+\mathrm{H}_2}$, $\sigma_{v,^{12}\mathrm{CO}(2-1)}$
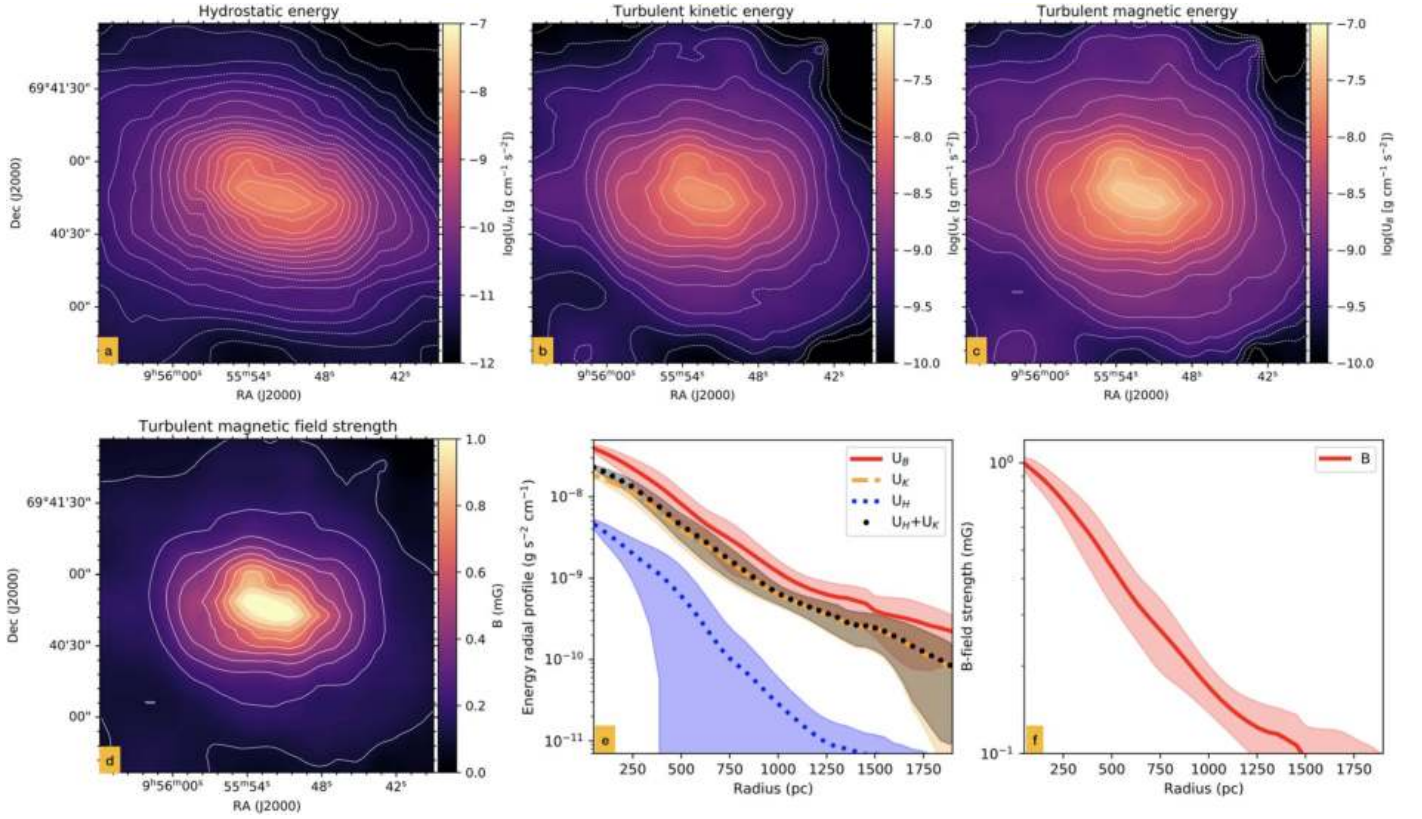
Figure 4. Hydrostatic (a), turbulent kinetic (b), and magnetic (c) energy maps within a $140'' \times 140''$ ($2.8 \times 2.8\ \mathrm{kpc}^2$) region. Contours start at -12 and increases in steps of 0.8 in logarithmic scale. (d) Turbulent magnetic field strength map. Contours start at 0.1 mG and increase in steps of 0.1 mG. Radial profiles of the energies (f) and turbulent magnetic field strength (f) showing the median (lines) and 1σ uncertainties (shaded region).

from Section 2, we compute the two-dimensional maps of the energies and turbulent magnetic field strength of M82. Figures 4(a)–(d) shows the resulting two-dimensional maps of the hydrostatic, turbulent kinetic, and turbulent magnetic energies as well as the turbulent magnetic field strength, each $140'' \times 140''$ ($2.8 \times 2.8\ \mathrm{kpc}^2$) in size. Figures 4(e) and (f) show the radial profiles of the energies and turbulent magnetic field strength. We estimate the median and standard deviation of the median (1σ) for an annulus of width equal to the Nyquist sampling ($2.43''$ and 48.5 pc) of the HAWC+ observations.

We find that the turbulent kinetic and turbulent magnetic energies are in close, within 1σ, equipartition across the galactic outflow at radius $\sim$300–1500 pc. At radius $\leqslant$300 pc, the turbulent magnetic energy appears to be higher than the turbulent kinetic energy. We note that this result within the starburst mask may imply that (1) the observed turbulent magnetic energy may be larger than the combined turbulent kinetic and hydrostatic energy in the compact star-forming regions, or (2) there may be several magnetic field components that may be overestimating the median turbulent magnetic field strength. A decomposition of the magnetic field strengths into small-scale turbulent fields (i.e., anisotropic random fields) due to star-forming regions or shocks in the superwind and large-scale fields due to galactic superwind are required to quantify the contribution of these several components to the observed magnetic field strength within the starburst mask (see Section 5.1). At radius $>$1500 pc, the turbulent kinetic energy shows a steeper drop than the turbulent magnetic energy; however, both energies still remain close to equipartition, within 1σ uncertainties.

Thompson et al. (2006) estimated the magnetic field strengths of starburst galaxies using a hydrostatic approach. These authors argued that the starbursts' magnetic field strengths are much larger than the magnetic field strengths inferred using the observed radio fluxes and assuming equipartition between cosmic rays and magnetic energy densities. These results are derived if the cosmic-ray electron cooling timescale is shorter than the escape timescale from the galactic disk. This work assumed that only the hydrostatic pressure takes place in the energy balance with the magnetic energy, which results in the scaling $B \propto \Sigma_g^a$, where Σ_g is the surface brightness of the gas, and a is the power-law index. $a = 0.7$ if the magnetic energy is in equipartition with the pressure from star formation in the ISM, and $a = 0.4$ for equipartition between cosmic rays and magnetic energy densities. Note that our magnetic field strength (Equation (19)) depends on the turbulent kinetic and hydrostatic energies, and it does not assume equipartition (β' is included).

4. Potential Field Extrapolation

We are interested in quantifying the influence of the galactic outflow in the magnetic field toward the IGM. This study requires the knowledge of the magnetic and kinetic energies at distances of several kiloparsecs from the galaxy plane. Although the kinetic energy can be estimated up to tens of kiloparsecs, there are no empirical measurements to compute the magnetic energies at these distances in M82. Our magnetic field results of M82 obtained in Section 3 provide an observational boundary condition required to perform a potential field extrapolation and estimate the field strength

and morphology at several kpc above and below the galactic plane.

We employ a standard, well-tested technique that has been used in solar physics for decades to determine the magnetic field in the solar corona, a region where the magnetic field (with rare exceptions) cannot be measured directly. In the solar physics case, the LOS magnetic field is measured in the photosphere using the Zeeman effect. This observation provides the first required boundary condition; the second condition assumes the field reduces to zero at infinity (see, e.g., Sakurai 1982). For a comprehensive review of magnetic field extrapolation techniques in solar physics please see Wiegelmann & Sakurai (2012). Potential field extrapolation has also been employed to study the magnetic field in slow-rotating and cool stars (Donati 2001; Hussain et al. 2001) such as τ Sco (Donati et al. 2006). Here, we have modified the solar physics method to work with POS polarization data from HAWC+.

4.1. Solving Laplace's Equation

The simplest of these extrapolation approximations assumes that the electrical currents are negligible. In this case, the magnetic field, $B = -\nabla\phi$, has a scalar potential, $\phi(x, y, z)$, that satisfies the Laplace equation (see *e.g.* Neukirch 2005)

$$\nabla^2\Phi = 0. \tag{20}$$

Here, the plane x–y is parallel to the galaxy's disk and our extrapolation will be limited to the x–z plane, above and below the galactic plane. This two-dimensional Cartesian geometry requires one boundary condition from the magnetic field map (Section 3) along the plane of the galaxy's disk at $xz = (x, 0)$

$$B_z(x, 0) = F(x) \tag{21}$$

and a second boundary condition at infinity, $B_z \to 0$ as $|z| \to \infty$. Using a separation of the variables

$$\Phi(x, z) = X(x)Z(z). \tag{22}$$

Substituting Equation (22) into Equation (20) gives

$$X''Z + XZ'' = 0. \tag{23}$$

A particular solution with wavenumber k has $X'' = -k^2X$ and $Z'' = k^2Z$, so

$$X(x) = A\cos(kx) + B\sin(kx), \tag{24}$$

$$Z(z) = Ce^{-k|z|} + De^{k|z|}, \tag{25}$$

where A, B, C, and D are constants. We now have

$$B_z = \frac{\partial\Phi}{\partial z} = X(x)(-Cke^{-k|z|} + Dke^{k|z|}), \tag{26}$$

As $B_z \to 0$ when $z \to \infty$, the constant $D = 0$. We can also set $C = 1$ as the constants can be set by the values of A and B. Then $Z(z) = e^{-k|z|}$, $X(x) = -F(x)/k$, and

$$\Phi_k = -\frac{1}{k}F(x)e^{-k|z|}. \tag{27}$$

We will assume that the source of $\vec{B}$ is finite, so that $B_z(x, 0) = F(x) = 0$ for $|x| > \ell/2$ for some length ℓ. We will also assume that the net flux into the upper half plane is zero, i.e.,

$$\int_{-\ell/2}^{\ell/2} F(x)dx = 0. \tag{28}$$

Expansion into a Fourier series gives

$$F(x) = \sum_{n=1}^{n=\infty} (a_n\cos k_n x + b_n\sin k_n x), \qquad k_n = \frac{2\pi n}{\ell}. \tag{29}$$

We now have

$$B_x(x, z) = \sum_{n=1}^{n=\infty} (a_n\sin k_n x - b_n\cos k_n x)e^{-k_n|z|}, \tag{30}$$

$$B_z(x, z) = \sum_{n=1}^{n=\infty} (a_n\cos k_n x + b_n\sin k_n x)e^{-k_n|z|}. \tag{31}$$

The coefficients are given by

$$a_n = \frac{2}{\ell}\int_{-\ell/2}^{\ell/2} F(x)\cos(k_n x)dx, \tag{32}$$

$$b_n = \frac{2}{\ell}\int_{-\ell/2}^{\ell/2} F(x)\sin(k_n x)dx. \tag{33}$$

Finally, the potential field orientations in the POS are estimated as

$$\phi = \arctan\left(\frac{B_z}{B_x}\right), \tag{34}$$

where the magnetic field components require to be projected on the observer's view given the inclination and tilt angle of the galaxy on the POS.

4.2. Potential Field Solutions

The boundary condition, $F(x)$, corresponds to the normal-to-plane component of the magnetic field (B_{norm}), so the observed POS magnetic field ($\boldsymbol{B}_{\mathrm{POS}}$) needs to be reprojected. We define the galaxy's plane by its tilt angle of $\theta = 64°$ measured as positive in the east from north direction (Mayya et al. 2005); this is designated by the black solid line in Figure 5. $\boldsymbol{B}_{\mathrm{POS}}$ corresponds to the measurements of the magnetic field strength (Figure 4(d)) and orientation (pseudo-vectors in Figure 5) along this line. We use Euler rotations around the x-axis, $R_x[i]$ and the z-axis, $R_z[\theta]$ to compute $\boldsymbol{B}_{\mathrm{norm}} = R_x[i]R_z[\theta]\boldsymbol{B}_{\mathrm{POS}}$ using an inclination angle of $i = 76°$ (Mayya et al. 2005) with respect to the LOS. $\boldsymbol{B}_{\mathrm{norm}}$ is displayed in Figure 5 as vectors along the galaxy's plane with lengths and color corresponding to their reprojected strength. In Figure 5 both *the* B_{POS} and B_{norm} strengths are seen as a function of the offset radius from the maximum of total intensity along the galaxy's plane.

It is important to recall here that magnetic field orientations determined by FIR polarimetric data suffer from the 180° ambiguity (Hildebrand et al. 2000)—that is, all vectors in Figure 5 (top) have the same likelihood to be pointing into the galaxy's plane. This angular ambiguity does not affect the shape or strength of the magnetic field lines, just the direction. Thus, we choose to calculate the potential field solution with this choice of direction for B_{norm} and only work with the orientation of the potential solutions.

Using the values of B_{norm} displayed in Figure 5 for the boundary condition $F(x)$, we can calculate the coefficients a_n and b_n in Equations (32) and (33) for $n = 1...500$ and $\ell = 1.2$ kpc (the extent of $F(x)$) using a trapezoidal method to evaluate the integral. Subsequently, we evaluate the potential field components in Equations (30) and (31) for x, $z = -11.45$–11.45 kpc. The resulting potential magnetic field lines are shown in Figure 6 within a 7.2×7.2 kpc^2 region
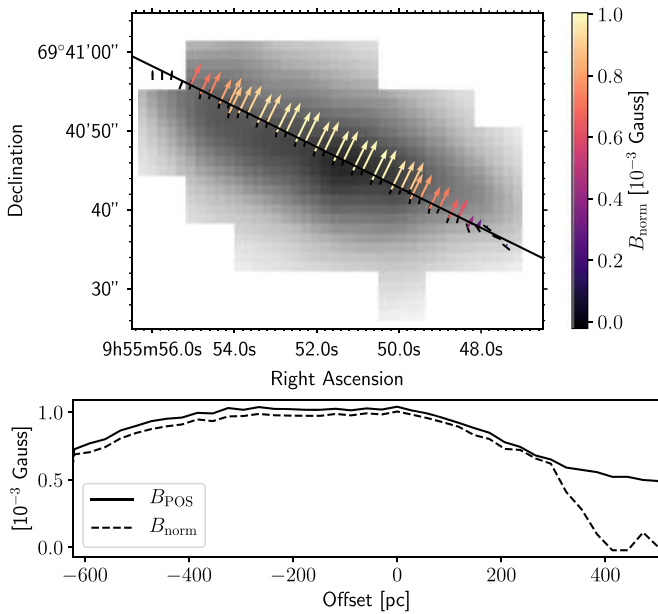
Figure 5. Top: boundary values B_{norm} for the potential field extrapolation in M82. B_{norm} vectors length and color correspond to the B_{POS} strength. The solid black line represents the plane of the galaxy defined at tilt angle 64° (Mayya et al. 2005). HAWC+ rotated polarization orientations (black) and arrows corresponding to the normal-to-plane component of the magnetic field (red) are shown along the galaxy's plane. Background corresponds to the total intensity at 53 μm. Bottom: B_{POS} (solid) and B_{norm} (dashed) profile as a function of the offset position from the maximum I intensity along the galaxy's plane.

centered at M82. Magnetic field lines are displayed in a gray scale that matches the potential field strength. Note that some lines appear truncated as an artifact of the line integration process performed by the Python package MATPLOTLIB (Hunter 2007). We display the potential field lines that originate from the empirical measurements using the 53 μm polarimetric observations with HAWC+. The maximum magnetic field strength of $\sim$1 mG seen in the bulk of the galaxy and the decrease to 100 μG at a radius of 1500 pc are in good agreement with the magnetic field strength estimated from HAWC+ data (Section 4.2).

Figure 7 displays a comparison between the orientations calculated with the potential field ($|\phi|$, Equation (34) (red) and measured with the HAWC+ instrument (black) for the central $\sim$700 × 700 pc^2 region of M82 where the total intensity $I > 0.5$ Jy arcec^{-2} and polarization fraction $P/\sigma_P > 3$ (the Chauvenet criteria). We measure an absolute angular difference (or misalignment) with a mean value of $16.3 \pm 25.6°$, where the maximum of occurrence is at $\sim$10.0°. Smaller angular differences ($<$10°) are located within the central $\sim$500 pc of the galaxy, above and below the plane. At these locations, the outflow dominates and the field orientation appears to be mainly poloidal. The strongest deviations are located on the far right and far left along the galactic plane. We find that the magnetic field is parallel to the galactic plane and outside the zone where the magnetic field is dragged by the superwind. Adebahr et al. (2017) also found a parallel magnetic field orientation in the western side of the galaxy (their labeled region 2), which is spatially coincident with ours. Early magnetic field models (i.e., Lesch et al. 1989) already accounted for these two components observed in radio observations (i.e., Reuter et al. 1992). Beck et al. (2019)
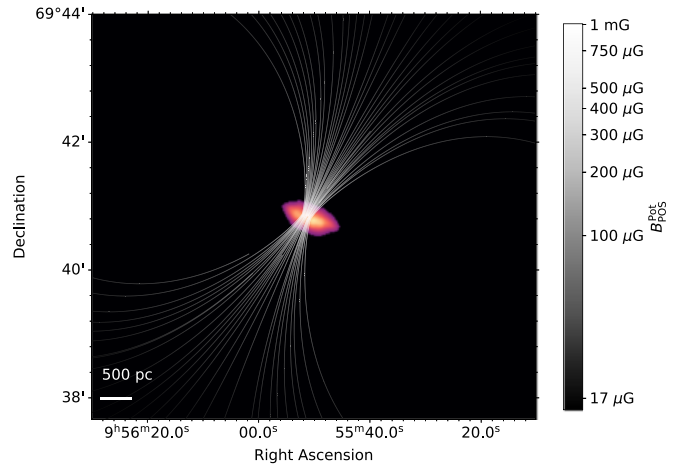

Figure 6. Potential magnetic field lines of M82 inferred using the 53 μm polarimetric observations with HAWC+/SOFIA. The potential magnetic field is calculated by extrapolation of the magnetic field at the galaxy's plane. Magnetic field lines are visualized in a field of view (FOV) $\sim$7.2 kpc^2 centered at M82. The potential field strength is larger in the bulk of the galaxy in good agreement with the 2D map of M82 in Figure 4.
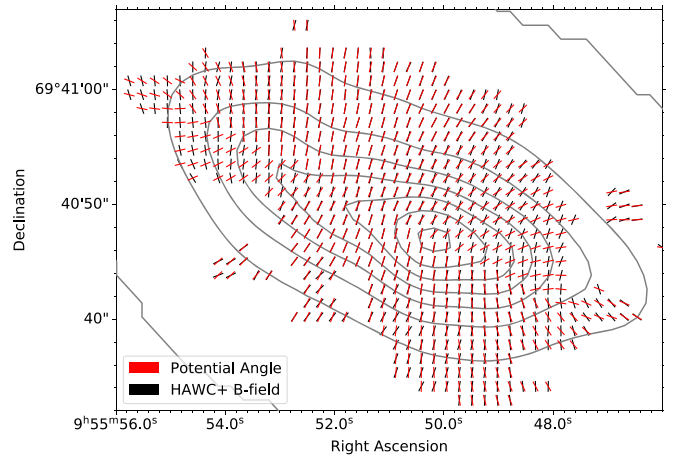

Figure 7. Comparison between the HAWC+ inferred magnetic field orientation (black) and the potential orientation (red) in locations of M82 with $I > 0.5$ Jy arcsec^{-2} and $p > 3\sigma_p$. Above and below the center of the galaxy's plane (where the outflow is observed) both orientations coincide, hinting that the poloidal-type of magnetic field is near a force-free configuration. Near the FIR edges orientations differ suggesting a non-potential configuration of the field. Grey contours in the background correspond to M82's FIR intensity values from HAWC+.

argued that dynamos are difficult to generate in starburst galaxies, as the dynamo growth rate is assumed to be shorter in starbursts than in regular galaxies. Thus, the magnetic field orientation along the galactic plane may be the remnant of the spiral magnetic field of M82 before the starburst stage.

5. Discussion

5.1. The Magnetic Fields in the Starburst Region

As noted in Section 3, the observed turbulent magnetic energy (U_B), is larger than the turbulent kinetic and hydrostatic energy ($U_K + U_H$) within the starburst mask (Figure 4). To investigate additional components in the observed turbulent magnetic energy within the central 2.8×2.8 kpc^2 region, we subtract the potential field magnetic energy from the observed
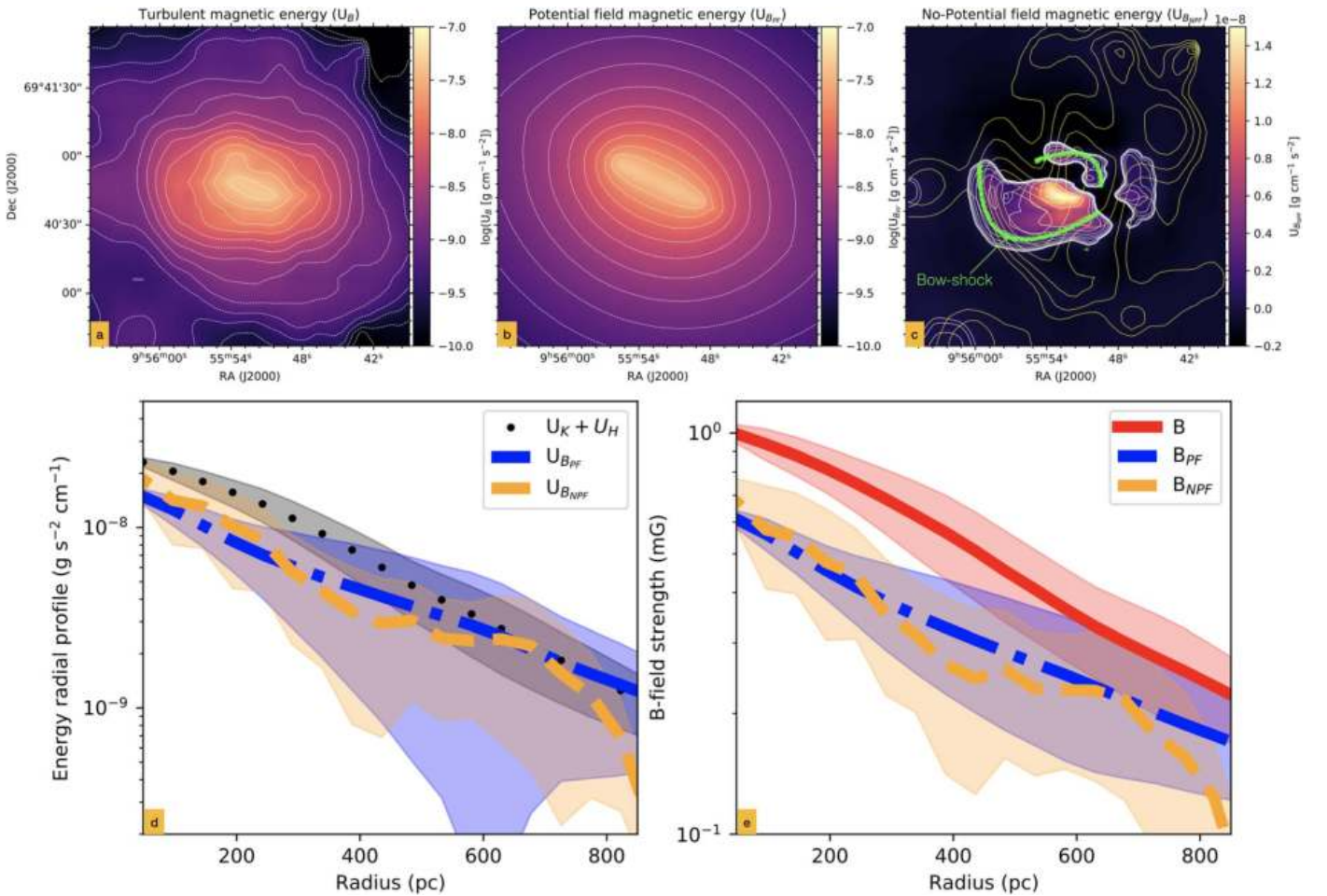
Figure 8. (a) The observed magnetic energy (U_B) is composed of (b) potential ($U_{B_{PF}}$) and (c) no-potential ($U_{B_{NPF}}$) field components. All energy maps with contours and FOV as in Figure 4. The no-potential field magnetic energy, $U_{B_{NPF}} = U_B - U_{B_{PF}}$, with overlaid ^{12}CO(2–1) velocity dispersion (yellow contours) is shown. The contours start at 50 km s^{-1} and increase in steps of 5 km s^{-1}. The bow-shock-like pattern (green) is identified. (d) The radial profiles of $U_K + U_H$, $U_{B_{NPF}}$, and corrected potential field, $U_{B_{PF}}$, energies with their associated magnetic field strengths in (e). The median (lines) and 1σ uncertainties are shown.

turbulent magnetic energy (Figure 8). The resulting map is labeled *non-potential* field, $U_{B_{NPF}} = U_B - U_{B_{PF}}$, which can be interpreted as a *residual* map of the observed minus model magnetic field energies. The non-potential map, $U_{B_{NPF}}$, has a *bow-shock-like* arc structure along the southeast and northwest regions of the outflow with an extension up to ∼600 pc from the core (Figure 8(c)). Shopbell & Bland-Hawthorn (1998) found a bow-shock arc at ∼500 pc in the southeast region of the outflow using [O III] and H$_\alpha$ emission lines. We find that the morphology of the non-potential field is similar to the morphology of the ^{12}CO(2–1) velocity dispersion. The increase of velocity dispersion corresponds to a higher non-potential magnetic energy. The southeast region has a higher contribution to the magnetic energy than the northwest region. The northwest region is viewed through the galactic disk, so this region of the outflow may be highly extinguished, make it appear less pronounced along the LOS. The bow-shock-like structure may be the wave front of the galactic outflow expanding through the IGM. This result represents the first direct detection of the turbulent magnetic energy generated by a bow shock in the galactic outflow of M82.

We conclude that the observed turbulent magnetic field energy within the starburst region is composed of two magnetic field components. A potential, large-scale (anisotropic turbulent or random) magnetic field from the galactic outflow, and a small-scale turbulent magnetic field (i.e., non-potential field) from a bow-shock-like region. The large-scale (anisotropic turbulent or random) B-field is thought to be generated by the galactic wind at scales equal to or larger than the turbulent coherent length ($\delta = 73.6 \pm 5.6$ pc). The small-scale turbulent B-field is thought to be generated by the turbulent or random fields in the the bow-shock-like structure at scales smaller than δ.

The observed turbulent magnetic energy has potential (large-scale) and non-potential (small-scale) components, $U_B = U_{B_{PF}} + U_{B_{NPF}}$. Figure 8(d) shows the radial profiles of $U_K + U_H$, U_{BPF}, and $U_{B_{NPF}}$. Note that the non-potential magnetic energy (yellow) drops precipitously at a radius of 900 pc. The magnetic fields associated to these energies are shown in Figure 8(e). We estimate that the non-potential and potential magnetic energies contribute $40 \pm 5\%$ and $53 \pm 4\%$ to the observed turbulent magnetic energy, respectively. Using these relative contributions, we estimate a median magnetic field strength of $305 \pm 15\,\mu$G and $222 \pm 19\,\mu$G for the potential field and non-potential magnetic field strength components, respectively.

Radio polarimetric observations using VLA and WSRT estimated a turbulent magnetic field strength in the range of 117–140 μG in the central 1×0.7 kpc^2 of M82 (Adebahr et al. 2017). This magnetic field strength was estimated assuming

equipartition between cosmic-ray energies and magnetic field energies from Beck & Krause (2005). As the ionized gas is likely to be inhomogeneous in the starbursts' region, Lacki (2013a, 2013b) accounted for the influence of giant star formation regions on the filing factor and radio luminosity. Specifically, uniform and discrete distribution of H II regions provides a high-density and low-filling-factor medium, which will raise the average density and turbulent energy densities. Within the starburst volume, the filing factor is estimated to be in the range of 0.1%–1% (Lacki 2013b, and references therein), which may introduce an uncertainty in the estimation of the gas turbulent energies up to an order of magnitude. Lacki (2013b) suggested a magnetic field strength of $\sim300\,\mu$G for M82 assuming a supernova-driven turbulence outflow, which lead to a close equipartition between the ISM components within the starburst—the turbulent energy density is comparable to the magnetic energy density in the starburst volume. To explain such a high magnetic field strength at radio wavelengths, Adebahr et al. (2013, 2017) suggested that there may be a superposition of at least two different phases of the magnetized medium at the core of M82—A strong milligauss field arising from the compact star-forming regions, and a weak diffuse microgauss component surrounding it. One of the main arguments for a two-component field in M82 are the high synchrotron losses electrons would experience, which would lead to a non-visible radio halo at radio wavelengths (Reuter et al. 1992; Adebahr et al. 2013). This revision was suggested by Thompson et al. (2006), who estimated a maximum B-field strength of 1.6 mG for the starburst of M82 from an equipartition analysis between the magnetic energy density and the hydrostatic ISM pressure. Lacki & Beck (2013) estimated a magnetic field strength of 220–240 μG using a revised equipartition due to strong energy losses in the dense cores of starburst galaxies.

The two-component scenario is similar to that measured in dense molecular clouds toward the Galactic center, where Zeeman splitting observations of OH masers indicate strong magnetic fields up to few milligauss (e.g., Yusef-Zadeh et al. 1996), while radio polarimetric observations reveal lower values of 50–100 μG (e.g., Crocker et al. 2010). Current FIR polarimetric observations at 53 μm from HAWC+ of the Galactic center region using an approach similar to the one presented here estimate magnetic field strengths of approximately a milligauss (Dowell et al., in preparation). From theoretical developments of the evolution of particles in the outflow of M82, Yoast-Hull et al. (2013) estimated a B-field strength in the range of 225–350 μG, while Paglione & Abrahams (2012) found a best-fit model with magnetic field strengths of 450 μG. The difference resides in the mean gas densities of 280–415 cm^{-3} for the former and 100–1000 cm^{-3} for the latter. Our results show that the milligauss component arises from the star-forming region (potential field) and the small-scale turbulent field from the bow-shock-like feature (non-potential field) within the central 900 pc of M82. Further models would require detail analysis of both components to explain the production of high-energy particles, formation of galactic winds, and generation of galactic shocks.

5.2. Open versus Closed Magnetic Field Lines

We investigate whether the potential magnetic field lines of M82 are *open* (i.e., galactic outflows) or *closed* (i.e., galactic fountains). We have revised the definitions from solar physics

(i.e., Levine et al. 1977; Fisk & Schwadron 2001) to apply to galactic winds. Open magnetic field lines remain attached to the central starburst and extend to large distances from the galactic plane. The turbulent kinetic energy of the outflowing wind exceeds the restoring turbulent magnetic energy. Field lines reaching these distances are dragged radially outward by the outflowing wind. Open field lines thus provide the missing link between the galaxies and IGM. Closed field lines remain attached to the central starburst and loop back to the plane of the galaxy. The turbulent magnetic energy exceeds the turbulent kinetic energy of the outflowing wind. Closed field lines provide a feedback channel from the central starburst back to the host galaxy.

We have shown that the turbulent kinetic and turbulent magnetic energies are in close equipartition up to ~2 kpc (Figure 4 and Section 3). It is important to note that the field lines may have a complex morphology within the starburst region at higher angular resolution than those from our observations. The averaged orientation of the turbulent magnetic field appears as ordered and fairly parallel to the outflow lines, but there may be many reversals or loops at smaller scales. From observational results, however, the field lines appear to remain open up to ~2 kpc.

The outflow of M82 extends at least ~11 kpc from the galactic plane (i.e., Devine & Bally 1999), at which distance some potential field lines may turn over and reconnect with the galactic plane. A magnetic field line will only serve as a channel for feedback if its strength is large enough to confine the ionized material to move along it. We find a striking similarity between the orientation of the observed B-field and potential field extrapolation, and the gas streams in MHD simulations using TNG50 (see Figure 12 by Nelson et al. 2019) or galactic outflows driven by supernovae. This result implies that the potential magnetic field is frozen in where the field lines are aligned with the outflowing wind. So do the magnetic field lines remain open at ~10 kpc or do they turn over at a height above ~2 kpc?

We can answer this question by comparing the kinetic and magnetic energies at such distances. To estimate the turbulent kinetic energy at distances of several kiloparsecs, the measurements of the dispersion velocity and mass density are required. HI observations of the M81 triplet covering an area of $3° \times 3°$ at a resolution of $20''$ (400 pc) provides a velocity dispersion of 35 ± 10 km s^{-1} at 6.6 kpc from M82 (de Blok et al. 2018). Martini et al. (2018) estimated that dusty clouds in the outflow are embedded in an ambient medium. The cloud particle density is $n_H^c = 10$ cm^{-3} ($\rho = 1.67 \times 10^{-23}$ g cm^{-3}), while the ambient particle density is $n_H^a = 0.044$ cm^{-3} ($\rho = 7.36 \times 10^{-26}$ g cm^{-3}). Using Equation (17), we estimate turbulent kinetic energies of $U_K^c = 3.07 \times 10^{-10}$ g s^{-2} cm^{-1} and $U_K^a = 1.35 \times 10^{-12}$ g s^{-2} cm^{-1} for the clouds and ambient medium, respectively.

Using the results of the potential field extrapolation, we estimate a magnetic field strength at radius $\geqslant 6.6$ kpc of $B_{PF} \leqslant 15$ μG, yielding $U_{B_{PF}} \leqslant 8.9 \times 10^{-12}$ g s^{-2} cm^{-1}. Magnetic field strengths up to 50 μG at scales of ~8 kpc in M82 has been measured using radio polarimetric observations and justified in terms of magnetized galactic winds (i.e., Kronberg et al. 1999). Basu & Roy (2013) used radio polarimetric observations to estimate B-field strengths of $\sim10\,\mu$G at a distance of ~10 kpc in several nearby normal spiral galaxies assuming equipartition of energy between
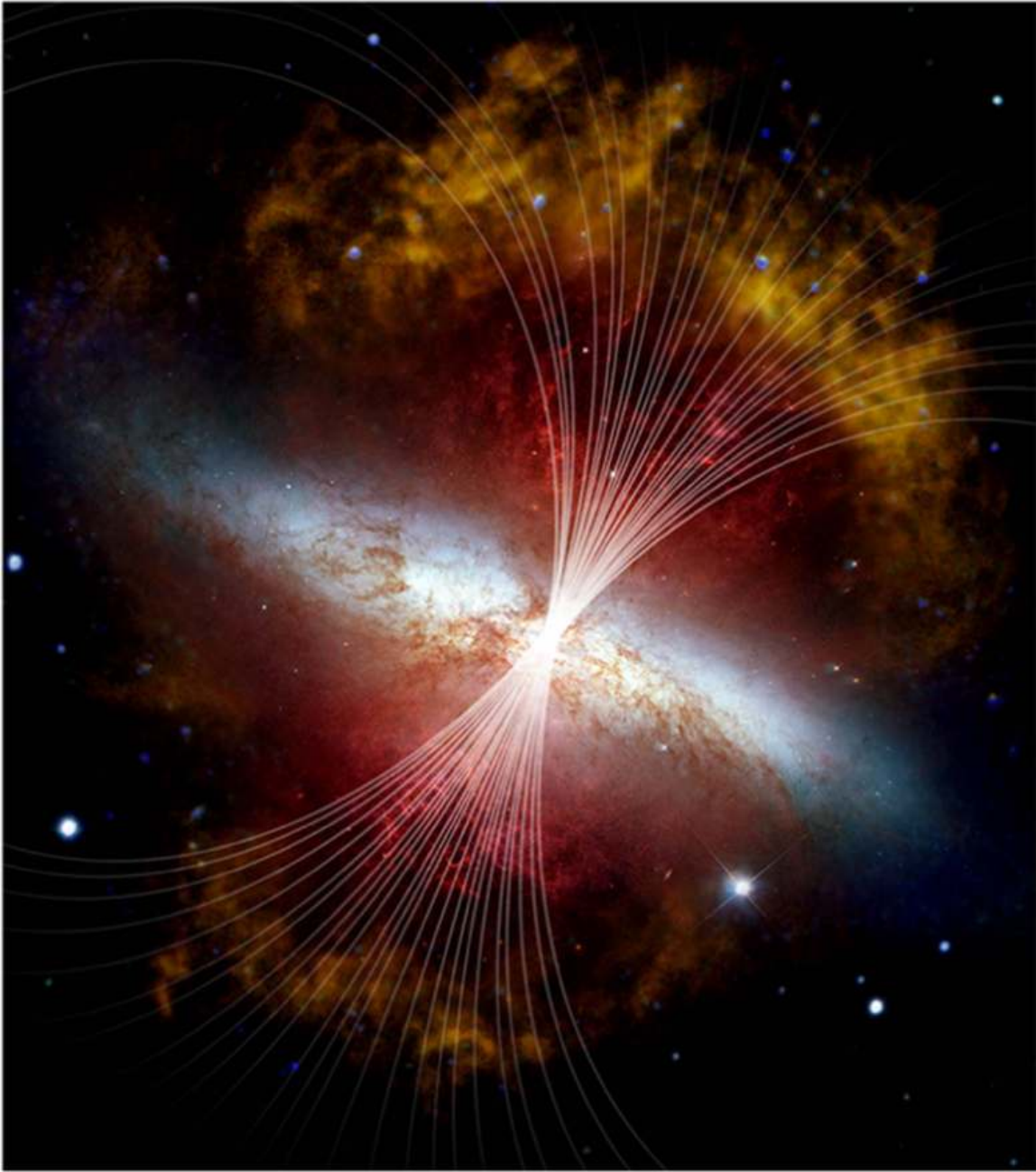
Figure 9. Composite image of M82 displaying the potential magnetic field lines. The starburst activity is seen in white light and the high-speed galactic outflow (red) in Hα emission, both by the Hubble Space Telescope (HST). In dark yellow, dust observed with Spitzer. Potential field lines, in white, are seen vanished at $r \approx 7$ kpc, as they are considered as open (galactic outflow).

cosmic-ray particles and magnetic fields. We estimate that $U_{B_{PF}} \sim U_K^a < U_K^c$ in the outflow at scales up to 6.6 kpc. We find that the dusty clouds are dominated by the kinetic energy in the outflowing wind, while the ambient medium is in close equipartition with the magnetic energy. Since the turbulent kinetic energy dominate the dusty medium, we conclude that the field lines are open at distances up to 6.6 kpc from the plane of M82, channeling magnetic energy and matter into the IGM (Figure 9).

Magnetic field strengths in the range of 2–40 μG have been measured in clusters on scales of 3–10 kpc through Faraday rotation measurements (i.e., Dreher et al. 1987; Kim et al. 1990; Taylor & Perley 1993; Clarke et al. 2001). These magnetic fields may be primordial, seeded in the IGM from shock waves or linked with the formation and evolution of galaxies (Subramanian 2019). Using semi-analytic simulations of magnetized galactic winds, Bertone et al. (2006) and Samui et al. (2018) suggested that galactic outflows may be able to seed a fraction of the magnetic field in the intracluster medium.

6. Conclusions

We used the HAWC+ polarimetric data as well as median values of the mass density, ρ, and the velocity dispersion, $\sigma_{v,^{12}CO(2-1)}$, from the literature to estimate the average POS magnetic field strength in the starburst region of M82 to be $B = 1.04 \pm 0.17$ mG (DCF and angular dispersion method).

12

We described a novel approach to quantify the turbulent magnetic field when large-scale flows are present (Section 2.3). We modified the DCF method to account for galactic superwind by adding a steady-flow term to the wave equation, which reverts to the traditional approach when large-scale flows are negligible. After we accounted for the large-scale flow, the median magnetic field within the starburst region is reduced to $B = 0.77 \pm 0.17$ mG.

We defined the turbulent plasma beta, β', as the ratio of hydrostatic-plus-turbulent kinetic pressure to magnetic pressure and, using median values within the starburst mask with a size of 873×510 pc^2 from Section 2, estimate $\beta' = 0.56 \pm 0.23$. The turbulent magnetic field energy is larger than the turbulent kinetic energy within the starburst. We can then use the pixel-by-pixel values of the density and velocity dispersion to construct, for the first time, a two-dimensional map of the turbulent magnetic field strength within the central 2.8×2.8 kpc^2 region of M82 (Figure 4(d)).

We modified the solar potential field method to work with galactic outflows using HAWC+ polarization data. We extrapolated the magnetic field from the core using the Laplace equation and investigate the potential magnetic structures along the galactic outflow of M82. The resulting potential magnetic field structure is shown in Figure 6. These results indicate that the observed turbulent magnetic field energy within the starburst region is composed of two components: a large-scale (anisotropic turbulent) field arising from the galactic outflow and a small-scale turbulent field arising from a bow-shock-like region. This result represents the first detection of the magnetic energy from a bow shock in the galactic outflow of M82.

The results of the potential field extrapolation allow us to determine, for the first time, if the field lines are open (i.e., galactic outflow) or closed (i.e., galactic fountain). We show that the turbulent kinetic and turbulent magnetic energies are in close equipartition up to $\sim$2 kpc (measured), while the turbulent kinetic energy dominates at $\sim$7 kpc (extrapolated). We estimated a magnetic field strength $\leqslant 15\ \mu$G at distances $\geqslant 6.6$ kpc from the starburst region. We conclude that the magnetic field lines associated with the galactic superwind of M82 are open, channeling matter into the galactic halo and beyond. These observations indicate that the powerful winds associated with the starburst phenomenon could be responsible for injecting material enriched with elements like carbon and oxygen into the IGM.

We demonstrated that FIR polarization observations are a powerful tool to study the B-field morphology in the cold and dense ISM of galactic outflows. Ongoing efforts like the SOFIA Legacy Program (PIs: Lopez-Rodriguez & Mao) focused on studying extragalactic magnetism will provide deeper observations at 53 μm to analyze the large-scale magnetic field in the disk of M82 as well as other nearby galaxies. The results presented here can also be used to investigate the high-energy particle production from starburst galaxies. This work serves as a strong reminder of the potential importance of magnetic fields, often completely overlooked, in the formation and evolution of galaxies.

ORCID iDs

Enrique Lopez-Rodriguez ⓘ https://orcid.org/0000-0001-5357-6538
Jordan A. Guerra ⓘ https://orcid.org/0000-0001-8819-9648
Mahboubeh Asgari-Targhi ⓘ https://orcid.org/0000-0003-0204-8385

References

Adebahr, B., Krause, M., Klein, U., et al. 2013, A&A, 555, A23
Adebahr, B., Krause, M., Klein, U., Heald, G., & Dettmar, R. J. 2017, A&A, 608, A29
Aitken, D. K., Smith, C. H., Moore, T. J. T., & Roche, P. F. 1998, MNRAS, 299, 743
Astropy Collaboration, Price-Whelan, A. M., Sipőcz, B. M., et al. 2018, AJ, 156, 123
Astropy Collaboration, Robitaille, T. P., Tollerud, E. J., et al. 2013, A&A, 558, A33
Attard, M., Houde, M., Novak, G., et al. 2009, ApJ, 702, 1584
Basu, A., & Roy, S. 2013, MNRAS, 433, 1675
Beck, R., Chamandy, L., Elson, E., & Blackman, E. G. 2019, Galax, 8, 4
Beck, R., & Krause, M. 2005, AN, 326, 414
Bertone, S., Vogt, C., & Enßlin, T. 2006, MNRAS, 370, 319
Brandenburg, A., & Subramanian, K. 2005, PhR, 417, 1
Cashman, L. R., & Clemens, D. P. 2014, ApJ, 793, 126
Chandrasekhar, S., & Fermi, E. 1953, ApJ, 118, 113
Chapman, N. L., Goldsmith, P. F., Pineda, J. L., et al. 2011, ApJ, 741, 21
Chisholm, J., & Matsushita, S. 2016, ApJ, 830, 72
Chrysostomou, A., Hough, J. H., Burton, M. G., & Tamura, M. 1994, MNRAS, 268, 325
Chuss, D. T., Andersson, B. G., Bally, J., et al. 2019, ApJ, 872, 187
Clarke, T. E., Kronberg, P. P., & Böhringer, H. 2001, ApJL, 547, L111
Contursi, A., Poglitsch, A., Graciá Carpio, J., et al. 2013, A&A, 549, A118
Cortes, P. C., Parra, R., Cortes, J. R., & Hardy, E. 2010, A&A, 519, A35
Crocker, R. M., Jones, D. I., Melia, F., Ott, J., & Protheroe, R. J. 2010, Natur, 463, 65
Crutcher, R. M. 2012, ARA&A, 50, 29
Davis, C. J., Chrysostomou, A., Matthews, H. E., Jenness, T., & Ray, T. P. 2000, ApJL, 530, L115
Davis, L. 1951, Phys. Rev., 81, 890
de Blok, W. J. G., Walter, F., Ferguson, A. M. N., et al. 2018, ApJ, 865, 26
Devine, D., & Bally, J. 1999, ApJ, 510, 197
Donati, J. F. 2001, in Astromography (Lecture Notes in Physics), Vol. 573, ed. H. M. J. Boffin et al. (Berlin: Springer)
Donati, J. F., Howarth, I. D., Jardine, M. M., et al. 2006, MNRAS, 370, 629
Dowell, C. D., Cook, B. T., Harper, D. A., et al. 2010, Proc. SPIE, 7735, 77356H
Dreher, J. W., Carilli, C. L., & Perley, R. A. 1987, ApJ, 316, 611
Elmegreen, B. G., & Scalo, J. 2004, ARA&A, 42, 211
Engelbracht, C. W., Kundurthy, P., Gordon, K. D., et al. 2006, ApJL, 642, L127
Fisk, L. A., & Schwadron, N. A. 2001, ApJ, 560, 425
Girart, J. M., Frau, P., Zhang, Q., et al. 2013, ApJ, 772, 69
Gonatas, D. P., Engargiola, G. A., Hildebrand, R. H., et al. 1990, ApJ, 357, 132
Greaves, J. S., Holland, W. S., Jenness, T., & Hawarden, T. G. 2000, Natur, 404, 732
Guerra, J. A., Chuss, D. T., Dowell, C. D., et al. 2021, ApJ, 908, 98
Harper, D. A., Runyan, M. C., Dowell, C. D., et al. 2018, JAI, 7, 1840008
Harris, C. R., Millman, K. J., van der Walt, S. J., et al. 2020, Natur, 585, 357
Haverkorn, M., Brown, J. C., Gaensler, B. M., & McClure-Griffiths, N. M. 2008, ApJ, 680, 362

Heckman, T. M., & Thompson, T. A. 2017, in Galactic Winds and the Role Played by Massive Stars, ed. A. W. Alsabti & P. Murdin (Berlin: Springer), 2431

Henning, T., Wolf, S., Launhardt, R., & Waters, R. 2001, ApJ, 561, 871

Hildebrand, R. H., Davidson, J. A., Dotson, J. L., et al. 2000, PASP, 112, 1215

Hildebrand, R. H., Kirby, L., Dotson, J. L., Houde, M., & Vaillancourt, J. E. 2009, ApJ, 696, 567

Houde, M., Fletcher, A., Beck, R., et al. 2013, ApJ, 766, 49

Houde, M., Hull, C. L. H., Plambeck, R. L., Vaillancourt, J. E., & Hildebrand, R. H. 2016, ApJ, 820, 38

Houde, M., Rao, R., Vaillancourt, J. E., & Hildebrand, R. H. 2011, ApJ, 733, 109

Houde, M., Vaillancourt, J. E., Hildebrand, R. H., Chitsazzadeh, S., & Kirby, L. 2009, ApJ, 706, 1504

Hunter, J. D. 2007, CSE, 9, 90

Hussain, G. A. J., Jardine, M., & Collier Cameron, A. 2001, MNRAS, 322, 681

Jones, T. J. 2000, AJ, 120, 2920

Jones, T. J., Dowell, C. D., Lopez Rodriguez, E., et al. 2019, ApJL, 870, L9

Kim, K. T., Kronberg, P. P., Dewdney, P. E., & Landecker, T. L. 1990, ApJ, 355, 29

Kronberg, P. P., Lesch, H., & Hopp, U. 1999, ApJ, 511, 56

Lacki, B. C. 2013a, MNRAS, 431, 3003

Lacki, B. C. 2013b, arXiv:1308.5232

Lacki, B. C., & Beck, R. 2013, MNRAS, 430, 3171

Leach, R. W., Clemens, D. P., Kane, B. D., & Barvainis, R. 1991, ApJ, 370, 257

Lehnert, M. D., Heckman, T. M., & Weaver, K. A. 1999, ApJ, 523, 575

Leroy, A. K., Walter, F., Martini, P., et al. 2015, ApJ, 814, 83

Lesch, H., Crusius, A., Schlickeiser, R., & Wielebinski, R. 1989, A&A, 217, 99

Levine, R. H., Altschuler, M. D., Harvey, J. W., & Jackson, B. V. 1977, ApJ, 215, 636

López-Coto, R., & Giacinti, G. 2018, MNRAS, 479, 4526

Lopez-Rodriguez, E., Alonso-Herrero, A., García-Burillo, S., et al. 2020, ApJ, 893, 33

Lopez-Rodriguez, E., Packham, C., Jones, T. J., et al. 2015, MNRAS, 452, 1902

Lopez-Rodriguez, E., Packham, C., Young, S., et al. 2013, MNRAS, 431, 2723

Martini, P., Leroy, A. K., Mangum, J. G., et al. 2018, ApJ, 856, 61

Matthews, B. C., McPhee, C. A., Fissel, L. M., & Curran, R. L. 2009, ApJS, 182, 143

Mayya, Y. D., Carrasco, L., & Luna, A. 2005, ApJL, 628, L33

McKinney, W. 2010, in Proc. of the 9th Python in Science Conf., ed. S. van der Walt & J. Millman, 56

Michail, J. M., Ashton, P. C., Berthoud, M. G., et al. 2021, ApJ, 907, 46

Minchin, N. R., & Murray, A. G. 1994, A&A, 286, 579

Morris, M., Davidson, J. A., Werner, M., et al. 1992, ApJL, 399, L63

Nakariakov, V. M., Roberts, B., & Murawski, K. 1998, A&A, 332, 795

Nelson, D., Pillepich, A., Springel, V., et al. 2019, MNRAS, 490, 3234

Neukirch, T. 2005, in Proc. of the Int. Scientific Conf. on Chromospheric and Coronal Magnetic Fields, ESA SP-596, ed. D. E. Innes et al., 596 (Nordwijk: ESA), 12.1

Ohyama, Y., Taniguchi, Y., Iye, M., et al. 2002, PASJ, 54, 891

Ostriker, E. C., Stone, J. M., & Gammie, C. F. 2001, ApJ, 546, 980

Paglione, T. A. D., & Abrahams, R. D. 2012, ApJ, 755, 106

Pattle, K., Ward-Thompson, D., Berry, D., et al. 2017, ApJ, 846, 122

Redaelli, E., Alves, F. O., Santos, F. P., & Caselli, P. 2019, A&A, 631, A154

Reuter, H. P., Klein, U., Lesch, H., Wielebinski, R., & Kronberg, P. P. 1992, A&A, 256, 10

Reuter, H. P., Klein, U., Lesch, H., Wielebinski, R., & Kronberg, P. P. 1994, A&A, 282, 724

Robitaille, T., & Bressert, E. 2012, APLpy: Astronomical Plotting Library in Python, ascl:1208.017

Ruzmaikin, A., Sokolov, D., & Shukurov, A. 1988, Natur, 336, 341

Sakurai, T. 1982, SoPh, 76, 301

Samui, S., Subramanian, K., & Srianand, R. 2018, MNRAS, 476, 1680

Schmelz, J. T., Holman, G. D., Brosius, J. W., & Willson, R. F. 1994, ApJ, 434, 786

Schmidt, H. U. 1964, in Proc. of the AAS-NASA Symp. 50, The Physics of Solar Flares, ed. W. N. Hess (Washington, DC: NASA), 107

Schmidt, T. 1970, A&A, 6, 294

Shapiro, P. R., Clocchiatti, A., & Kang, H. 1992, ApJ, 389, 269

Shopbell, P. L., & Bland-Hawthorn, J. 1998, ApJ, 493, 129

Soam, A., Liu, T., Andersson, B. G., et al. 2019, ApJ, 883, 95

Sohn, J., Ann, H. B., Pak, S., & Lee, H. M. 2001, JKAS, 34, 17

Stephens, I. W., Looney, L. W., Kwon, W., et al. 2013, ApJL, 769, L15

Subramanian, K. 2019, Galax, 7, 47

Tadaki, K., Iono, D., Yun, M. S., et al. 2018, Natur, 560, 613

Taylor, G. B., & Perley, R. A. 1993, ApJ, 416, 554

Thompson, T. A., Quataert, E., Waxman, E., Murray, N., & Martin, C. L. 2006, ApJ, 645, 186

Vacca, W. D., Hamilton, R. T., Savage, M., et al. 2015, ApJ, 804, 66

Vaillancourt, J. E., Chuss, D. T., Crutcher, R. M., et al. 2007, Proc. SPIE, 6678, 66780D

Van Rossum, G., & Drake, F. L. 2009, Python 3 Reference Manual (Scotts Valley, CA: CreateSpace)

Wang, J.-W., Koch, P. M., Galván-Madrid, R., et al. 2020, ApJ, 905, 158

Wentzel, D. G. 1963, ARA&A, 1, 195

Wiegelmann, T., & Sakurai, T. 2012, LRSP, 9, 5

Yoast-Hull, T. M., Everett, J. E., Gallagher, J. S. I., & Zweibel, E. G. 2013, ApJ, 768, 53

Yusef-Zadeh, F., Roberts, D. A., Goss, W. M., Frail, D. A., & Green, A. J. 1996, ApJL, 466, L25

Zielinski, N., Wolf, S., & Brunngräber, R. 2021, A&A, 645, A125

Zweibel, E. G. 1990, ApJ, 362, 545